Physics in Medicine & Biology

IPEM Institute of Physics and Engineering in Medicine

PAPER • OPEN ACCESS

Positron range-free and multi-isotope tomography of positron emitters

To cite this article: F J Beekman *et al* 2021 *Phys. Med. Biol.* **66** 065011

Physics in Medicine & Biology

IPEM Institute of Physics and Engineering in Medicine

OPEN ACCESS

RECEIVED
10 November 2020

REVISED
5 February 2021

ACCEPTED FOR PUBLICATION
12 February 2021

PUBLISHED
4 March 2021

PAPER

Positron range-free and multi-isotope tomography of positron emitters

F J Beekman[1,2,3], **C Kamphuis**[2,3], **S Koustoulidou**[2,4], **R M Ramakers**[1,2,3] **and M C Goorden**[1]

[1] Department of Radiation Science and Technology, Delft University of Technology, Mekelweg 15, 2629 JB Delft, The Netherlands
[2] MILabs B.V., Heidelberglaan 100, 3584 CX, Utrecht, The Netherlands
[3] Department of Translational Neuroscience, Brain Center Rudolf Magnus, University Medical Center Utrecht, The Netherlands
[4] Department of Radiology and Nuclear Medicine, Erasmus MC, 3015 CN, Rotterdam, The Netherlands

E-mail: f.j.beekman@tudelft.nl

Keywords: multi-isotope PET, positron-range free PET, PET-SPECT, high-energy PET, preclinical PET, micro-PET, SPECT

Abstract

Despite improvements in small animal PET instruments, many tracers cannot be imaged at sufficiently high resolutions due to positron range, while multi-tracer PET is hampered by the fact that all annihilation photons have equal energies. Here we realize multi-isotope and sub-mm resolution PET of isotopes with several mm positron range by utilizing prompt gamma photons that are commonly neglected. A PET-SPECT-CT scanner (VECTor/CT, MILabs, The Netherlands) equipped with a high-energy cluster-pinhole collimator was used to image ^{124}I and a mix of ^{124}I and ^{18}F in phantoms and mice. In addition to positrons (mean range 3.4 mm) ^{124}I emits large amounts of 603 keV prompt gammas that—aided by excellent energy discrimination of NaI—were selected to reconstruct ^{124}I images that are unaffected by positron range. Photons detected in the 511 keV window were used to reconstruct ^{18}F images. Images were reconstructed iteratively using an energy dependent matrix for each isotope. Correction of ^{18}F images for contamination with ^{124}I annihilation photons was performed by Monte Carlo based range modelling and scaling of the ^{124}I prompt gamma image before subtracting it from the ^{18}F image. Additionally, prompt gamma imaging was tested for ^{89}Zr that emits very high-energy prompts (909 keV). In Derenzo resolution phantoms 0.75 mm rods were clearly discernable for ^{124}I, ^{89}Zr and for simultaneously acquired ^{124}I and ^{18}F imaging. Image quantification in phantoms with reservoirs filled with both ^{124}I and ^{18}F showed excellent separation of isotopes and high quantitative accuracy. Mouse imaging showed uptake of ^{124}I in tiny thyroid parts and simultaneously injected ^{18}F-NaF in bone structures. The ability to obtain PET images at sub-mm resolution both for isotopes with several mm positron range and for multi-isotope PET adds to many other unique capabilities of VECTor's clustered pinhole imaging, including simultaneous sub-mm PET-SPECT and theranostic high energy SPECT.

1. Introduction

Preclinical PET and SPECT scanners are important devices for basic and translational research. The mouse is the most commonly used experimental animal due to its high similarity with the human homolog, today's existence of many mature genetic manipulation techniques, ease of fast breading and availability of economical housing. Typically, clinical scanners have resolutions ranging from 3 to 6 mm for PET and 8–10 mm for SPECT. As most mouse organs are roughly an order of magnitude smaller than their human counterparts, sub-mm resolution is required to measure molecule concentrations in similar sub-structures in organs and tumors. Preclinical SPECT most often relies on pinhole collimation and nowadays some systems reach resolutions down to a quarter mm *in vivo* (Ivashchenko *et al* 2015). Like clinical PET, preclinical PET is commonly based on coincidence detection of photons resulting from annihilation of an emitted positron with an electron in neighboring tissue. Resolutions down to 0.8 mm have been reported in high-end commercial coincidence PET systems (Yang *et al* 2004, Miyaoka *et al* 2004, Rouze *et al* 2004, Tai *et al* 2005) but only for isotopes with very small positron ranges

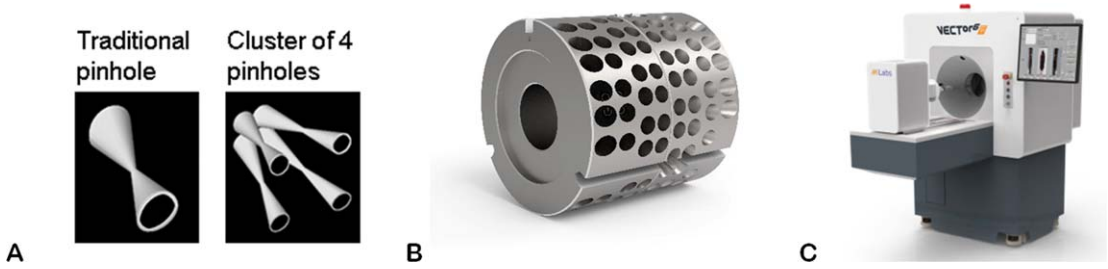

Figure 1. (A) Cluster of pinholes versus traditional pinhole. (B) clustered multi-pinhole collimator. Reproduced from Goorden *et al* 2020. © 2020 Institute of Physics and Engineering in Medicine. All rights reserved. (C) VECTor^{6}CT system. Reproduced with permission from MIlabs.

Table 1. Positron ranges, half-lives, gamma energies and abundancies for several relevant PET isotopes (e.g. from (Le Loirec and Champion 2007a, 2007b, 2007c, Laforest and Liu 2009)). All isotopes in this table already have medical applications (Andreyev and Celler; Conti and Eriksson 2016).

Isotope	Positron range (Mean)	Positron range (Max)	Half-life	Probability positron emission	Energy and probability gamma emission
^{68}Ga	3.56 mm	10.3 mm	67.8 min	88.9%	1077 keV (3.2%)
^{76}Br	2.47 mm	20.2 mm	16.2 h	54.8%	559 keV (74%)
					657 keV (15.9%)
^{82}Rb	7.49 mm	18.6 mm	1.3 min	95.4%	777 keV (15.1%)
^{86}Y	2.51 mm	11.1 mm	14.7 h	31.9%	1077 keV (82.5%)
					627 keV (32.6%)
^{124}I	3.37 mm	11.7 mm	100.2 h	22.7%	603 keV (62.9%)
					1691 keV (11.2%)
^{89}Zr	1.27mm	4.21 mm	78.4 h	22.7%	909 keV (99%)
^{38}K	5.67 mm	15.3 mm	7.61 m	99%	2170 keV (99%)
^{44}Sc	2.46 mm	7.36 mm	3.97 h	94.3%	1157 keV (100%)
^{52m}Mn	5.29 mm	14.5 mm	21.1 m	98%	1434 keV (98%)
^{60}Cu	4.13 mm	21.0 mm	23.4 m	92.5%	826 keV (21%)
					1332 keV (88%)
					1792 keV (46%)
^{72}As	5.19 mm	18.2 mm	26 h	88%	833 keV (815)

like ^{18}F. For a recent research prototype small field-of-view coincidence PET system dedicated to mouse brain imaging, a 0.6 mm resolution was reported (Yang *et al* 2016).

Many image degrading effects inherent to coincidence PET which play a relatively small role in human imaging become disturbing in small animals. Important factors in this regard are detector blurring, including depth-of-interaction (DOI) effects, and detection of random and scattered photons (Goorden and Beekman 2010, Goorden *et al* 2013). To reduce their impact, high-performance PET requires very expensive detector technology which can limit its practical application. For some isotopes an even more important image degrading effect is the positron range (e.g. 3.4 mm mean/ 11.7 mm max for ^{124}I, see table 1) resulting in significant losses in resolution and quantitative accuracy. Like other blurring effects these can be partly recovered using advanced iterative methods, but this requires accurate knowledge of tissue boundaries, e.g. from precisely aligned and preprocessed MRI or CT data (Cal-Gonzalez *et al* 2015). One should note that the shape of the 3D positron range kernel is highly peaked with long tails, which results in better small hot lesion visibility than would be the case for a Gaussian-like blurring kernel with the same mean range but that this on the other hand can cause more challenging quantification issues.

Earlier we have launched a method for simultaneous and sub-mm PET-SPECT imaging based on clustered pinhole collimation, named Versatile Emission Computed Tomography (VECTor (Goorden *et al* 2013, Walker *et al* 2014)). Due to the use of (i) clustered pinhole—rather than electronic-collimation (figure 1(A and B)) and (ii) gamma detectors with good energy resolution (8% at 511 keV), several image degrading effects inherent to electronic collimation are dramatically reduced or eliminated; for example scatter contamination in the photopeak is much lower, while detector blur and DOI have far less impact on resolution because of strong pinhole image magnification. At the same time, highly degrading noise equivalent count-rate effects caused by randoms and coincidence losses that severely affect coincidence PET are eliminated with clustered pinhole PET. Therefore, despite the lower number of photons detected with VECTor, it can for many cases outperform

coincidence PET in terms of image resolution and image contrast to noise ratio, particularly in organ and tumor imaging (Walker *et al* 2014). Unique capabilities of VECTor (figure 1(C)) include (i) performing sub-mm resolution PET and SPECT simultaneously, (ii) sub-mm resolution imaging of therapeutic isotopes that emit high energy gammas such as ^{213}Bi (440 keV) (de Swart *et al* 2016) and ^{131}I (364 keV) (van der Have *et al* 2016), and (iii) providing an ultra-high resolution nuclear imaging platform with adaptable resolution-sensitivity trade-off e.g. through use of exchangeable collimators with application-specific pinhole diameters and geometries. As a consequence, this technology is already in use for a wide range of applications (e.g. (Walker *et al* 2014, Miwa *et al* 2015, de Swart *et al* 2016, van der Have *et al* 2016, Adachi *et al* 2017, Esquinas *et al* 2017, Robertson *et al* 2017, Chacko *et al* 2017, Verhoog *et al* 2018, Chekol *et al* 2018, Knight *et al* 2019a, Knight *et al* 2019b, Wilson *et al* 2019)).

Thus far, the above-mentioned positron range effect degrades VECTor's resolution as it does in coincidence PET. With VECTor often an equivalent SPECT isotope can be used as a work around (like ^{67}Ga instead of ^{68}Ga, ^{123}I, ^{125}I or ^{131}I instead of ^{124}I, and ^{111}In instead of ^{89}Zr), isotopes which can all be imaged at sub-half-mm resolution. Here an additional option is presented in case one wants or needs to stick to PET isotopes, allowing for high-resolution imaging of long positron range isotopes. This option is enabled by VECTor's unique collimation technique and relies on the fact that several PET isotopes with long positron ranges also emit significant amounts of gammas straight from the atom (see table 1 showing that there are quite a number of such isotopes).

Another unmet need is to routinely create multi-isotope PET images. For coincidence PET systems thus far, two main methods have been proposed. A first method uses the difference in half-lives and kinetic behavior of different tracers, sometimes combined with staggered injection to separate their time-activity-curves (Rust *et al* 2006, Kadrmas *et al* 2013, Verhaeghe and Reader 2013). This has been applied in animal models (Black *et al* 2008, Figueiras *et al* 2011, Cheng *et al* 2015, Bell *et al* 2017) and patients (Joshi *et al* 2009, Zhang *et al* 2016). It relies on many assumptions about the pharmacokinetics of radiotracers or their spatial distribution and it has been pointed out that this is not actual simultaneous multi-tracer imaging (Fukuchi *et al* 2017) such as is for example done with SPECT systems that discriminate gammas emitted by different isotopes based on their energies. A second method is simultaneous imaging of a pure positron emitter and a positron emitter co-emitting prompt gammas (Andreyev and Celler 2011, Gonzalez *et al* 2011, Andreyev *et al* 2014). The development of a small-animal multi-isotope PET based on this principle was reported recently (Fukuchi *et al* 2017). This method has the disadvantage that it requires modifications to the scanner's electronics to detect three gammas in coincidence and that a large number of quite bulky additional gamma detectors need to be added to reach a reasonable sensitivity for the scarce triple coincidences. In addition, the method works only for those PET isotopes that emit a high energy gamma *simultaneously* with a positron; it is therefore unsuited for delayed gammas or in cases when a large number of emitted gammas is not associated with positron decay but with electron capture.

The aim of the present paper is to (i) describe initial results of VECTor's capabilities of imaging isotopes with several mm positron range at sub-mm resolution and (ii) demonstrate simultaneous sub-mm imaging of different PET isotopes. Both new imaging capabilities are based on utilizing high-energy prompt or delayed gammas. Note that while VECTor uses gammas directly emitted by the isotope, it does not require triple coincidence and thus both delayed as well as prompt gammas not associated with positron emission can be utilized. In this paper we demonstrate these capabilities for the PET isotopes ^{89}Zr and ^{124}I in combination with ^{18}F. Thus, positron range-free PET and dual-isotope PET are achieved by acquiring magnified multi-pinhole projections in the extremely high energy domain with a commercially available PET-SPECT-CT scanner.

2. Materials and methods

2.1. Data acquisition

Animal and phantom scans were performed using a PET-SPECT-CT scanner (VECTor^{6}CT, MILabs B.V.) equipped with three stationary large NaI(Tl) gamma detectors (595 × 472, 9.5 mm crystal thickness) and a dedicated high energy mouse collimator (HE-UHR-M) with 144 pinholes (0.7 mm diameter each) organized in clusters of four (Goorden *et al* 2013). Images were acquired as list mode data meaning that estimated energy of each detected photon was stored. The advantage of this capability is that energy windows can be selected retrospectively.

2.2. *In vivo* animal imaging

All animal studies were performed in accordance with the Dutch Law on Animal Experimentation and all protocols were approved by the Animal Research Committee of the University Medical Center Utrecht. Healthy C57BL/6 mice (20–25 g body weight) were injected i.v. in the tail vein with 12 MBq of ^{124}I-NaI and 118 MBq of

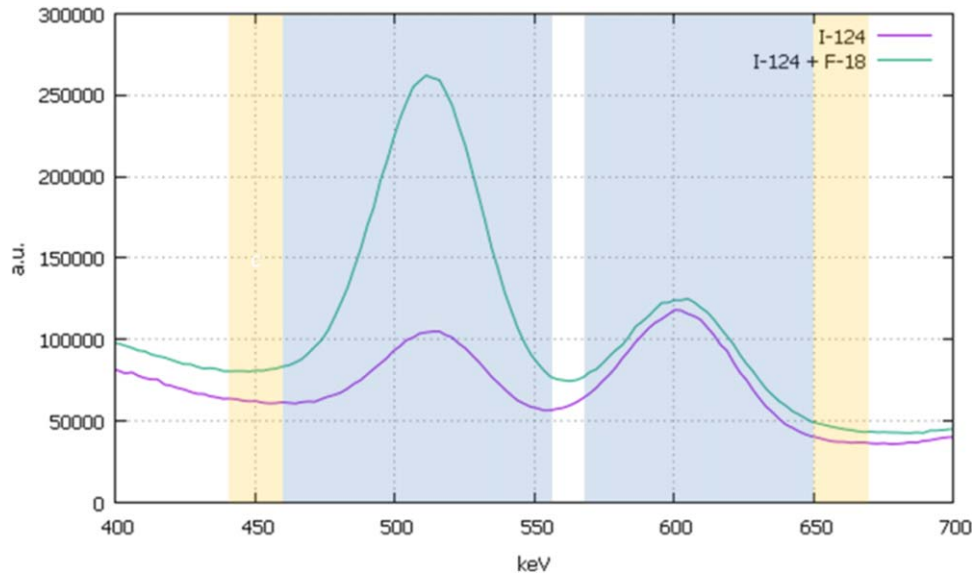

Figure 2. Energy spectrum for a ^{18}F/^{124}I mix including the energy windows used.

^{18}F-NaF, 24 h and 115 min before the scan started respectively. The animals were anesthetized using 2% of isoflurane in air and the tracer distributions were imaged simultaneously for 60 min.

2.3. Phantom imaging

A Derenzo phantom, containing 6 sectors of rods with varying diameter (0.45, 0.50, 0.55, 0.75, 0.80 and 0.85 mm) was used for resolution measurements. Per sector the rod diameters were equal to the distance between them. The phantom was filled with an initial activity of 29.9 MBq of ^{124}I and 29.9 MBq of ^{18}F and scanned continuously for ten half-lives of ^{18}F. For each half-life time scan, the first 30 min were reconstructed to obtain a series of images with different amounts of ^{18}F. To additionally emulate the measurement of lower doses of ^{124}I, the list mode data of the last frame with completely decayed ^{18}F was reduced by a factor that equals the fraction of the real dose and the emulated dose by randomly removing events from the list mode data. Additionally, single isotope ^{124}I Derenzo images were acquired with 26 MBq ^{124}I and a scan time of 30 min.

A cylindrical phantom (diameter 22 mm) containing three tubes (500 μl per tube, inner diameter 6.5 mm) was imaged to assess quantitative accuracy. In this scan of 30 min, one tube contained 0.98 MBq of ^{124}I, a second tube was filled with 10.1 MBq of ^{18}F, and the remaining tube contained a mix of 0.98 MBq of ^{124}I and 10.1 MBq of ^{18}F.

Images of a second Derenzo phantom (rod sizes of 0.70, 0.75, 0.80, 0.90, 1.00 and 1.20 mm) were acquired with an initial dose of 40 MBq ^{89}Zr and scan time of 30 min.

2.4. Image reconstruction

All images were reconstructed by a combined dual-matrix dual-voxel pixel-based (Branderhorst *et al* 2010) similarity regulated (Vaissier *et al* 2016) OSEM (DM-SR-OSEM) algorithm. Dual-matrix image reconstruction (Zeng and Gullberg 1997) uses different matrices for forward projection and back projection to accelerate reconstruction. In our case, the back projection step did not contain positron range blurring and included only part of the photons penetrating the collimator (for details see (Goorden *et al* 2020)). Dual-voxel reconstruction is an acceleration technique (Goorden *et al* 2020) that uses larger voxels for the low frequency tail part of the point spread functions in the forward projection. MC-generated detector PSFs including Compton scatter were used. A triple energy window scatter and cross talk correction (Ogawa *et al* 1991) was used and was modified for this specific case of dual-isotope imaging (see figure 2). For ^{18}F imaging, photons in the 511 keV photopeak (461–561 keV) were used as well as 2 background subtraction windows (441–461 keV/ 650–670 keV). For ^{124}I imaging, the 609 keV photopeak (570−650 keV) was used with one background window (650–670 keV). For ^{89}Zr imaging, reconstructions from (i) the 511 keV photopeak (461–561 keV) and (ii) the 909 keV photopeak (841−977 keV) were compared. Scatter was corrected by using a triple energy window with a width of 2.5% each on each side of the 15% wide peak window.

Separate matrices were used to model the energy specific photon transport through collimator and detector material for 511, 603 or 909 keV photons. Matrices were obtained by raytracing to model the pinhole penetration and detector interaction for the specified energy, while calibration was based on ^{99m}Tc point source

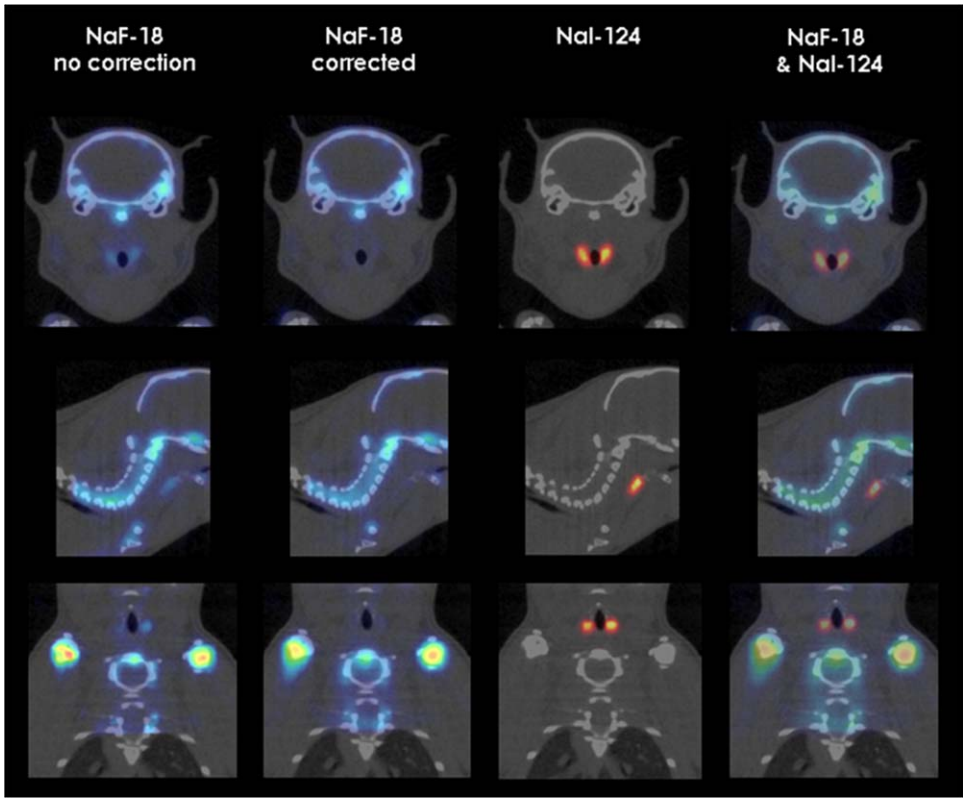

Figure 3. Simultaneous dual isotope mouse images with ^{18}F-NaF and ^{124}I-NaI (12 MBq and 55 MBq resp. at start) overlaid with x-ray CT images. Top: Transaxial slices. Center: Sagittal slices. Bottom: coronal slices. Left and 2nd column: ^{18}F-NaF image uncorrected and corrected for down scatter and annihilation photons originating from ^{124}I-NaI. Third Column: ^{124}I-NaI image from 603 keV prompt photons showing small details from the thyroid. Right Column: Corrected ^{18}F-NaF and ^{124}I-NaI image merged.

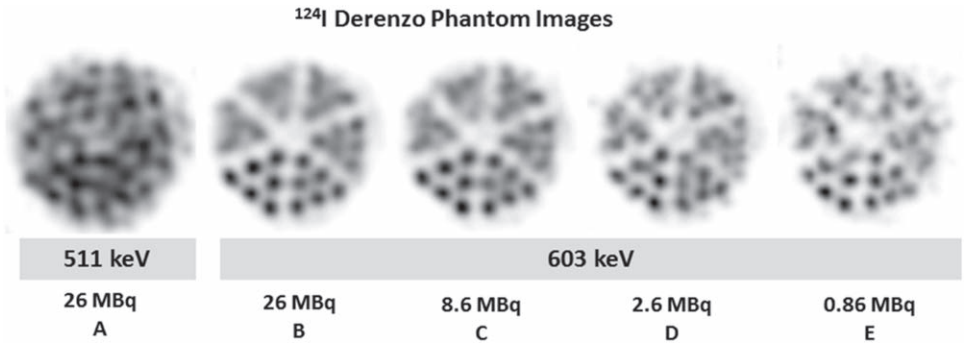

Figure 4. Images of Derenzo phantom (rod sizes 0.45, 0.50, 0.55, 0.75, 0.80 and 0.85 mm) filled with different amounts of ^{124}I and scanned for 30 min. (A) Reconstruction from 511 keV annihilation photons. (B)–(E) Prompt images at different activity levels (up to a factor of 30 difference with frames A and B).

measurements (Goorden *et al* 2016). For absolute quantitative imaging a calibration method based on a single cup of activity was used. This was applied to each isotope with single isotope imaging (Wu *et al* 2011).

2.5. Calibration for cross talk correction

For ^{124}I imaging only the 603 keV prompt gammas were selected, while the 511 keV photons were not used because of the enormous positron range. When ^{18}F is imaged simultaneously with ^{124}I using the 511 keV channel, one in fact creates images that represent positron annihilations of both isotopes where the ^{124}I image is heavily blurred by positron range effects. To correct the ^{18}F image for this effect we calculated an estimate of the amount of contamination of ^{124}I present in the ^{18}F image with the following method. First positron range blurring was applied to the positron range-free 603 keV ^{124}I image using pre-calculated and normalized Gate Monte Carlo simulation (Jan *et al* 2004) generated kernels. This blurred image was subsequently scaled and subtracted from a 511 keV ^{124}I only image determined experimentally from phantom experiments. The scaling

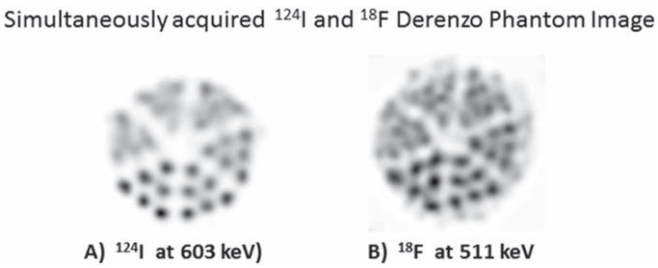

Figure 5. Derenzo phantom (rod sizes 0.45, 0.50, 0.55, 0.75, 0.80 and 0.85 mm), activity ratio ^{124}I : ^{18}F equals 1:1. (A) ^{124}I image. (B) 511 keV ^{18}F image corrected for ^{124}I annihilation photons.

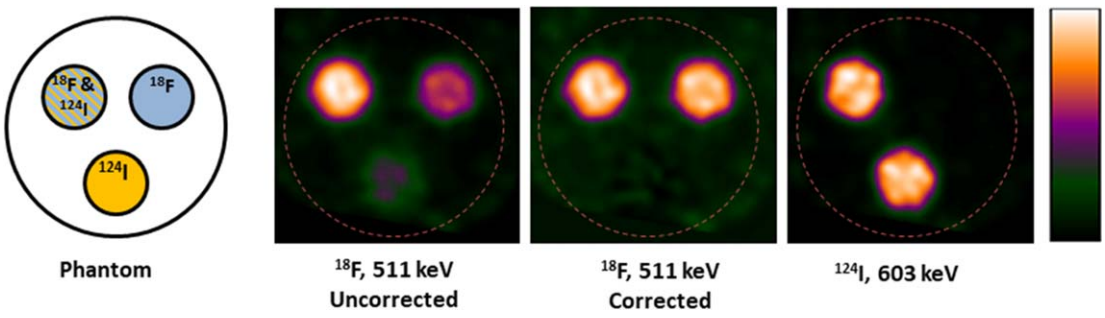

Figure 6. Quantification phantom with 3 compartments filled according to the concentrations provided in table 2. This table also shows that the quantitative accuracy for ^{124}I is excellent and that after correction for ^{124}I cross talk the same holds true for ^{18}F.

factor was considered to be optimal when after subtraction there are zero counts left. The scaling factor found this way was 0.87. Using this scaling factor ^{18}F images obtained from dual-isotope ^{18}F/^{124}I imaging were corrected by subtracting the estimated contamination of ^{124}I.

3. Results

Figure 3 shows images of the mouse co-injected with ^{124}I-NaI and ^{18}F-NaF. The activities at the time of imaging were 12 MBq and 55 MBq respectively. By only using the prompt gammas for ^{124}I-NaI reconstruction, the 3.4 mm average positron range of ^{124}I can be avoided and structures smaller than a mm in the mouse thyroid can be easily resolved. Correction of ^{18}F-NaF images is necessary to remove contamination from the ^{124}I-NaI distribution from the images. Images were reconstructed using 50 iterations DM-SR-OSEM and 3D Gaussian post-filtered with FWHM $=$ 0.6 mm.

Figure 4 shows the difference between ^{124}I reconstructions from 511 keV annihilation photon imaging (Frame A) and 603 keV photons (Frame B) at equal dose (images were reconstructed from the same scan). Frames B–E show the effect of count reduction corresponding to a range of activities between 26 MBq and 0.86 MBq (at the start of the scan). All images were reconstructed using 50 iterations DM-SR-OSEM and Gaussian post-filtered with a FWHM of 0.5 mm, 0.5 mm, 0.55 mm, 0.60 mm and 0.65 mm respectively to get proper visualization at the increasing noise level with lower activity.

Figure 5 shows simultaneous Dual-Isotope PET images of a Derenzo phantom filled with a mix of ^{124}I and ^{18}F discerning the 0.75 mm rods. Images were reconstructed using 50 iterations DM-SR-OSEM and Gaussian post-filtered (FWHM $=$ 0.5 mm). In the 511 keV photopeak the number of counts after background correction amounted to 72.0 M, which is the estimated number of primary counts from ^{18}F, and in the 603 keV window the number of counts after background correction amounted to 30.5 M.

Figure 6 shows the phantom with 3 compartments with (1) a ^{18}F/^{124}I mix of activity concentration ratio of 1:3.86, (2) ^{18}F only and (3) ^{124}I only. The amounts of activity were calculated from the images using cylindrical VOIs of 8 mm diameter and 30 mm length around the cups. Images were reconstructed using 50 iterations DM-SR-OSEM and 3D Gaussian post-filtered with an FWHM of 1 mm. Reconstructed amounts of ^{18}F in compartments (1) and (2) were found to be equal as was the amount of ^{124}I in compartments (1) and (3). The intensity images together with the ROI values in table 2 show that after correction, the quantitative accuracy is excellent. The activity in the filled compartments barely deviates from the true concentrations but for ^{18}F, application of cross talk correction is very important.

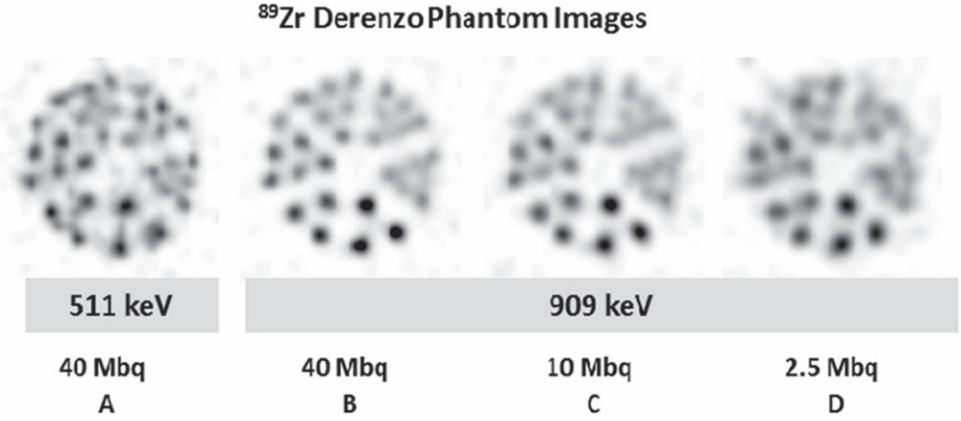

Figure 7. Derenzo phantom (rod diameters 1.2 1.0 0.9 0.8 0.75 0.7 mm) filled with ^{89}Zr. (A) image based on the use of 511 keV window, compared to (B) image from the 909 keV photopeak window. (C)–(D) Prompt images at lower activity levels (up till 16× lower than in frame A).

Table 2. Quantitative accuracy in cup phantom shown in figure 6 with ^{124}I only, ^{18}F only or a mix of both.

	Measured Concentration (MBq ml^{-1}) Uncorrected % Error	Measured Concentration (MBq ml^{-1}) Corrected % Error	True Concentration (MBq ml^{-1})
Compartment I			
^{18}F	0.54 (54%)	0.34 (3%)	0.35
^{124}I	1.42 (5%)	n.a.	1.35
Compartment II			
^{18}F	0.36 (3%)	0.34 (3%)	0.35
^{124}I	0.05 (4%)	n.a.	0.0
Compartment III			
^{18}F	0.21 (60%)	0.01 (3%)	0.0
^{124}I	1.42(5%)	n.a.	1.35

Figure 7 shows that also ^{89}Zr images can strongly improve in clarity when prompts are imaged instead of annihilation photons, despite the fact that the photon energies are almost 1 MeV. All images were reconstructed using 100 iterations DM-SR-OSEM and Gaussian post-filtered with a FWHM of 0.5 mm, 0.5 mm, 0.6 mm and.0.8 mm respectively to get proper visualization at the increasing noise level with lower activity. At 511 keV many rods are affected in shape by scatter and positron range although even 0.7 mm rods are visible, but 0.75 mm rods are not well discernable from each other. The rods at 909 keV are much rounder and therefore more realistic, but the 0.7 mm rods are hard to see at 909 keV which may be explained by a wider PSF at 909 keV due to e.g. pinhole edge penetration. It should be noted that scatter and the amount of counts play a big role in the quality of the 511 keV based images: for the 40 MBq scan in the 511 keV window the photopeak counts amounted 173 M but the estimated number of primary counts was 34.1 M after TEW correction. This is 3.35 times lower than the amount of estimated primary photons (again by TEW) of 114.5 M counts in the 909 keV window.

4. Discussion

We presented first results of positron range-free PET imaging based on imaging prompt gammas that are co-emitted with positrons by many PET isotopes and often have a considerable abundance (table 1). We tested this method for ^{124}I and ^{89}Zr and showed that for both isotopes 0.75 mm rods in a Derenzo resolution phantom could be clearly discerned (figures 4 and 7), which used to be impossible before. Since partial volume effects are a main hurdle for quantitative imaging, the presented method can be a great step forward to precise imaging of these isotopes. Since the presented work was carried out with an isotope with a large positron range (3.4 mm in average) for coincidence imaging, and one with an extremely high prompt energy (909 keV), we expect that many other applications with isotopes listed in table 1 can benefit from imaging the prompt gammas as well.

Also combining the information from all photopeaks (511 keV plus prompt gammas) may be interesting to further improve the results in some studies.

The current work was carried out with a VECTor system with rather thin crystals. Today these systems are also delivered with crystals that have more than 2.3 × higher capturing efficiency and are equipped with dedicated software that can model the increased DOI effects including Compton effects in the crystal. Such a scanner was not available to us in an animal lab at this stage of the research project. In addition, higher sensitivity collimators can be used which together would support much shorter scan times or lower doses than used in the present paper, albeit at the cost of some spatial resolution The loss of resolution can be partly compensated for by accurate modeling of the collimator in the system matrix that is used for reconstruction.

So far energy windows settings and image reconstruction have not yet been optimized. The optimal width of the windows may be dose dependent and using both the 511 keV window and window for prompt photons could be interesting when for each window the reconstruction matrix is optimized.

Simultaneous dual-isotope PET imaging is important since it can reduce scan time compared to two separate scans which can limit the time needed to keep the animal under anesthesia and it inherently results in perfectly registered images of different tracer molecules. The present work shows that such studies are feasible even based on simple cross talk correction.

5. Conclusion

This study showed that (i) sub-mm resolution imaging of a PET isotope with several mm mean positron range and (ii) simultaneous sub-mm resolution imaging of different PET isotopes is enabled by clustered pinhole collimation and magnification, using a system with stationary large field-of-view NaI detectors (VECTor) and dedicated image reconstruction methods. Many other PET isotopes with a large positron range also have also additional prompt gammas that can be imaged in this way. The use of a wide variety of PET tracers, including large positron-range PET isotopes, and mixes of multiple PET and SPECT tracers paves the way for many new imaging protocols in biomedical research.

Acknowledgments

This work financed by the research grant QUARAT: Quantitative Universal Radiotracer Tomography (TTW16885) which is financed in part by the Dutch Research Council (NWO).

References

Adachi N *et al* 2017 *In vivo* simultaneous imaging of vascular pool and hypoxia with a HT-29 tumor model: the application of dual-isotope SPECT/PET/CT *Int. J. Sci.* **25** 26–39

Andreyev A and Celler A 2011 Dual-isotope PET using positron-gamma emitters *Phys. Med. Biol.* **56** 4539–56

Andreyev A, Sitek A and Celler A 2014 EM reconstruction of dual isotope PET using staggered injections and prompt gamma positron emitters *Med. Phys.* **41**

Bell C, Puttick S, Rose S, Smith J, Thomas P and Dowson N 2017 Design and utilisation of protocols to characterise dynamic PET uptake of two tracers using basis pursuit *Phys. Med. Biol.* **62** 4897–916

Black N F, McJames S, Rust T C and Kadrmas D J 2008 Evaluation of rapid dual-tracer (62)Cu-PTSM + (62)Cu-ATSM PET in dogs with spontaneously occurring tumors *Phys. Med. Biol.* **53** 217–32

Branderhorst W, Vastenhouw B and Beekman F J 2010 Pixel-based subsets for rapid multi-pinhole SPECT reconstruction *Phys. Med. Biol.* **55** 2023–34

Cal-Gonzalez J, Perez-Liva M, Herraiz J L, Vaquero J J, Desco M and Udias J M 2015 Tissue-dependent and spatially-variant positron range correction in 3D PET *IEEE Trans. Med. Imaging* **34** 2394–403

Chacko A M *et al* 2017 F-18-FDG as an inflammation biomarker for imaging dengue virus infection and treatment response *JCI Insight* **2**

Chekol R *et al* 2018 (89)Zr-nimotuzumab for immunoPET imaging of epidermal growth factor receptor I *Oncotarget* **9** 17117–32

Cheng X Y, Li Z L, Liu Z, Navab N, Huang S C, Keller U, Ziegler S I and Shi K Y 2015 Direct parametric image reconstruction in reduced parameter space for rapid multi-tracer PET imaging *IEEE Trans. Med. Imaging* **34** 1498–512

Conti M and Eriksson L 2016 Physics of pure and non-pure positron emitters for PET: a review and a discussion *EJNMMI Phys.* **3** 8

de Swart J, Chan H S, Goorden M C, Morgenstern A, Bruchertseifer F, Beekman F J, de Jong M and Konijnenberg M W 2016 Utilizing high-energy gamma-photons for high-resolution Bi-213 SPECT in mice *J. Nucl. Med.* **57** 486–92

Esquinas P L, Rodriguez-Rodriguez C, Carlos De La Vega J, Bokharaei M, Saatchi K, Shirmohammad M, Hafeli U O, Sossi V and Celler A 2017 188 Re image performance assessment using small animal multi-pinhole SPECT/PET/CT system *Phys. Med.* **33** 26–37

Figueiras F P, Jimenez X, Pareto D, Gomez V, Llop J, Herance R, Rojas S and Gispert J D 2011 Simultaneous dual-tracer PET imaging of the rat brain and its application in the study of cerebral ischemia *Mol. Imaging Biol.* **13** 500–10

Fukuchi T, Okauchi T, Shigeta M, Yamamoto S, Watanabe Y and Enomoto S 2017 Positron emission tomography with additional gamma-ray detectors for multipletracer imaging *Med. Phys.* **44** 2257–66

Gonzalez E, Olcott P D, Bieniosek M and Levin C S 2011 Methods for increasing the sensitivity of simultaneous multi-isotope positron emission tomography *IEEE Nucl. Sci. Conf. R.* pp 3597–601

Goorden M C and Beekman F J 2010 High-resolution tomography of positron emitters with clustered pinhole SPECT *Phys. Med. Biol.* **55** 1265–77

Goorden M C, Kamphuis C, Ramakers R M and Beekman F J 2020 Accelerated image reconstruction by a combined dual-matrix dual-voxel approach *Phys. Med. Biol.* **65** 1–17
Goorden M C, van der Have F, Kreuger R, Ramakers R M, Vastenhouw B, Burbach J P H, Booij J, Molthoff C F M and Beekman F J 2013 VECTor: a preclinical imaging system for simultaneous submillimeter SPECT and PET *J. Nucl. Med.* **54** 306–12
Goorden M C, van Roosmalen J, van der Have F and Beekman F J 2016 Optimizing modelling in iterative image reconstruction for preclinical pinhole PET *Phys. Med. Biol.* **61** 3712–33
Ivashchenko O, van der Have F, Villena J L, Groen H C, Ramakers R M, Weinans H H and Beekman F J 2015 Quarter-millimeter-resolution molecular mouse imaging with U-SPECT(+) *Mol. Imaging* **14** 1–8
Jan S *et al* 2004 GATE: a simulation toolkit for PET and SPECT *Phys. Med. Biol.* **49** 4543–61
Joshi A D, Koeppe R A, Fessler J A and Kilbourn M R 2009 Signal separation and parameter estimation in noninvasive dual-tracer PET scans using reference-region approaches *J. Cereb. Blood Flow Metab.* **29** 1346–57
Kadrmas D J, Rust T C and Hoffman J M 2013 Single-scan dual-tracer FLT + FDG PET tumor characterization *Phys. Med. Biol.* **58** 429–49
Knight J C *et al* 2019a Early detection in a mouse model of pancreatic cancer by imaging DNA damage response signalling *J. Nucl. Med.* **61** 1006–13
Knight J C, Mosley M J, Kersemans V, Dias G M, Allen P D, Smart S and Cornelissen B 2019b Dual-isotope imaging allows *in vivo* immunohistochemistry using radiolabelled antibodies in tumours *Nucl. Med. Biol.* **70** 14–22
Laforest R and Liu X D 2009 Cascade removal and microPET imaging with Br-76 *Phys. Med. Biol.* **54** 1503–31
Le Loirec C and Champion C 2007a Track structure simulation for positron emitters of medical interest: I. The case of the allowed decay isotopes *Nucl. Instrum. Methods* A **582** 644–53
Le Loirec C and Champion C 2007b Track structure simulation for positron emitters of physical interest: II. The case of the radiometals *Nucl. Instrum. Methods* A **582** 654–64
Le Loirec C and Champion C 2007c Track structure simulation for positron emitters of physical interest: III. The case of the non-standard radionuclides *Nucl. Instrum. Methods* A **582** 665–72
Miwa K, Inubushi M, Takeuchi Y, Katafuchi T, Koizumi M, Saga T and Sasaki M 2015 Performance characteristics of a novel clustered multi-pinhole technology for simultaneous high-resolution SPECT/PET *Ann. Nucl. Med.* **29** 460–6
Miyaoka R S, Janes M L, Park B K, Lee K, Kinahan P E and Lewellen T K 2004 Toward the development of a micro crystal element scanner (MiCES): quickPET II *IEEE Nucl. Sci. Conf. R.* pp 2242–6
Ogawa K, Harata Y, Ichihara T, Kubo A and Hashimoto S 1991 A practical method for position-dependent Compton-scatter correction in single photon-emission ct *IEEE Trans. Med. Imaging* **10** 408–12
Robertson A K H, Ramogida C F, Rodriguez-Rodriguez C, Blinder S, Kunz P, Sossi V and Schaffer P 2017 Multi-isotope SPECT imaging of the 225Ac decay chain: feasibility studies *Phys. Med. Biol.* **62** 4406–20
Rouze N C, Schmand M, Siegel S and Hutchins G D 2004 Design of a small animal PET imaging system with 1 microliter volume resolution *IEEE Trans. Nucl. Sci.* **51** 757–63
Rust T C, DiBella E V, McGann C J, Christian P E, Hoffman J M and Kadrmas D J 2006 Rapid dual-injection single-scan 13N-ammonia PET for quantification of rest and stress myocardial blood flows *Phys. Med. Biol.* **51** 5347–62
Tai Y C, Ruangma A, Rowland D, Siegel S, Newport D F, Chow P L and Laforest R 2005 Performance evaluation of the microPET focus: a third-generation microPET scanner dedicated to animal imaging *J. Nucl. Med.* **46** 455–63
Vaissier P E B, Beekman F J and Goorden M C 2016 Similarity-regulation of OS-EM for accelerated SPECT reconstruction *Phys. Med. Biol.* **61** 4300–15
van der Have F, Ivashchenko O, Goorden M C, Ramakers R M and Beekman F J 2016 High-resolution clustered pinhole (131)Iodine SPECT imaging in mice *Nucl. Med. Biol.* **43** 506–11
Verhaeghe J and Reader A J 2013 Simultaneous water activation and glucose metabolic rate imaging with PET *Phys. Med. Biol.* **58** 393–411
Verhoog S, Kee C W, Wang Y, Khotavivattana T, Wilson T C, Kersemans V, Smart S, Tredwell M, Davis B G and Gouverneur V 2018 (18)F-Trifluoromethylation of Unmodified Peptides with 5-(18)F-(Trifluoromethyl)dibenzothiophenium Trifluoromethanesulfonate *J. Am. Chem. Soc.* **140** 1572–5
Walker M D, Goorden M C, Dinelle K, Ramakers R M, Blinder S, Shirmohammad M, van der Have F, Beekman F J and Sossi V 2014 Performance assessment of a preclinical PET scanner with pinhole collimation by comparison to a coincidence-based small-animal PET scanner *J. Nucl. Med.* **55** 1368–74
Wilson T C *et al* 2019 PET Imaging of PARP Expression Using (18)F-Olaparib *J. Nucl. Med.* **60** 504–10
Wu C, de Jong J R, van Andel H A G, van der Have F, Vastenhouw B, Laverman P, Boerman O C, Dierckx R A J O and Beekman F J 2011 Quantitative multi-pinhole small-animal SPECT: uniform versus non-uniform Chang attenuation correction *Phys. Med. Biol.* **56** N183–93
Yang Y F *et al* 2016 A prototype high-resolution small-animal PET scanner dedicated to mouse brain imaging *J. Nucl. Med.* **57** 1130–5
Yang Y F, Tai Y C, Siegel S, Newport D F, Bai B, Li Q Z, Leahy R M and Cherry S R 2004 Optimization and performance evaluation of the microPET II scanner for *in vivo* small-animal imaging *Phys. Med. Biol.* **49** 2527–45
Zeng G L and Gullberg G T 1997 On using an unmatched projector and backprojector pair in an iterative algorithm *J. Nucl. Med.* **38** 207–207
Zhang J L, Morey A M and Kadrmas D J 2016 Application of separable parameter space techniques to multi-tracer PET compartment modeling *Phys. Med. Biol.* **61** 1238–58